

# Mechanical origins of lithium-metal intrusions into garnet solid electrolytes revealed by failure statistics

Geoff McConohy<sup>1,4,5\*</sup>, Xin Xu<sup>1,4,5\*</sup>, Teng Cui<sup>2,5</sup>, Edward Barks<sup>1,4</sup>, Sunny Wang<sup>3,4</sup>, Emma Kaeli<sup>1</sup>, Celeste Melamed<sup>1</sup>, X. Wendy Gu<sup>2</sup>, William C. Chueh<sup>1,4\*</sup>

<sup>1</sup>Department of Materials Science and Engineering, Stanford University, Stanford, CA, USA

<sup>2</sup>Department of Mechanical Engineering, Stanford University, Stanford, CA, USA

<sup>3</sup>Department of Chemistry, Stanford University, Stanford, CA, USA

<sup>4</sup>Stanford Institute for Materials and Energy Sciences, SLAC National Accelerator Laboratory, Menlo Park, CA, USA

<sup>5</sup>These authors contributed equally to this work

\*Email: [mcconohy@stanford.edu](mailto:mcconohy@stanford.edu), [xinxu1@stanford.edu](mailto:xinxu1@stanford.edu), [wchueh@stanford.edu](mailto:wchueh@stanford.edu)

## Abstract

Solid-state electrolytes are an attractive option to increase the chemical stability and energy density of rechargeable lithium-metal batteries. However, they are susceptible to lithium-metal short-circuiting during charging, especially under high current densities. In this work, using a force-controlled electrical microprobe inside a focused-ion beam scanning electron microscope, we performed 48 experiments of electroplating lithium metal onto  $\text{Li}_{6.6}\text{La}_3\text{Ta}_{0.4}\text{Zr}_{1.6}\text{O}_{12}$  (LLZO) and observed the initiation of lithium penetration (termed intrusions) into the solid electrolyte, with and without externally applied stress. Employing a statistical approach, we find that the cumulative probability of intrusion as a function of lithium metal diameter follows a two-parameter Weibull distribution, implying defect-governed fracture behavior for the intrusion initiation. Upon applying a contact force of 5 mN with a 5-10  $\mu\text{m}$  microprobe, the characteristic failure diameter of lithium metal decreases by a factor of 2.6 due to the generation of nanoscale cracks as suggested by nanoindentation and finite element simulations. Furthermore, we introduce in-plane compressive strain to LLZO through a cantilever bending experiment and

demonstrate that strain as small as 0.067% strongly influences the direction of intrusion propagation immediately following initiation. Overall, our results suggest that both mechanically-generated and pre-existing defects as well as mechanical strain dominate the intrusion behavior in LLZO, a phenomenon that could extend to other solid electrolytes.

## Introduction

Lithium-metal penetration is one of the main modes of cell failure in solid-state batteries and limits the plating rate during charging<sup>1</sup>. While some researchers have described lithium-metal structures penetrating the electrolyte as “dendrites”, the morphology of the lithium metal is not necessarily tree-like<sup>2,3</sup>. As an alternative, we here use the term “intrusions”, defined as lithium-metal growth that electrochemically propagates within the solid-state electrolyte. Studying lithium-metal intrusions can aid in the development of inspection methods to screen out defective materials before they are incorporated into full devices. Further, a fundamental understanding of this intrusion process will enable the design of next-generation solid-state batteries that can remain stable over higher charge rates.

The mechanism of lithium-metal penetration into solid-state electrolytes has been an important topic of scientific research since the seminal work of Monroe and Newman<sup>4</sup>. They predicted that solid-state electrolytes with a shear modulus >8 GPa would suppress lithium metal intrusion due to the dependence of the electrochemical potential of lithium on stress<sup>4</sup>. However, one of the most studied oxide solid electrolytes, Li<sub>7</sub>La<sub>3</sub>Zr<sub>2</sub>O<sub>12</sub> (LLZO, which is usually doped with Al, Ta, or Ga), has a shear modulus of ~60 GPa<sup>5,6</sup> but still exhibits intrusion growth at current densities well below 1 mA cm<sup>-2</sup> (averaged across the electrode)<sup>2,7</sup>, which is even lower than the threshold current density for liquid electrolytes. Recent theoretical studies resolve this

contradiction by suggesting that the morphological instability of ceramic solid electrolytes is due to the low partial molar volume of lithium ions in the electrolyte<sup>8</sup>. Nonetheless, theoretical models based on bulk and homogenous material properties do not explain the wide variation of current densities at failure shown in the literature<sup>2</sup>. For example, while many authors report intrusions at current densities lower than 1 mA cm<sup>-2</sup>, others report ~10 mA cm<sup>-2</sup> with electrolyte surface treatment<sup>9,10</sup>, and some report over 100 mA cm<sup>-2</sup> without intrusion<sup>11</sup> for lithium microelectrodes. This wide range of current densities at failure suggests an incomplete understanding of intrusion growth in LLZO.

Other mechanisms have been proposed to explain how lithium intrusions develop and propagate in LLZO. Transmission electron microscopy (TEM) and X-ray photoelectron spectroscopy experiments have shown that LLZO is chemically stable to lithium metal<sup>12,13</sup>. As such, a coupled electro-chemo-mechanical intrusion mechanism, which has been observed in Li<sub>1+x</sub>Al<sub>x</sub>Ga<sub>2-x</sub>(PO<sub>4</sub>)<sub>3</sub><sup>14</sup> and Li<sub>10</sub>GeP<sub>2</sub>S<sub>12</sub><sup>15</sup>, is unlikely. The two mechanisms that have gained the most attention center on fracture mechanics and electronic conductivity. The fracture mechanics hypothesis posits that lithium metal builds up stress inside of pre-existing cracks and eventually causes fracture, similar to traditional brittle fracture<sup>16–18</sup>. Fracture events have been directly observed during lithium plating via scanning electron microscopy (SEM)<sup>11</sup> and optical microscopy<sup>3</sup>. Previous work relates the electrochemical driving forces to the size of the defects<sup>19–21</sup>, with literature dating back to the 1980s for β-alumina<sup>22,23</sup>, though quantitative experimental data (both electrochemical and mechanical) to verify these models is sparse. Alternatively, the electronic conductivity hypothesis proposes that a small leakage of electrons into the solid electrolyte causes lithium metal to plate internally (i.e. without a direct connection to the surface lithium), which eventually short circuits the cell<sup>24–26</sup>. We note that internal plating in the bulk of

transparent LLZO was not directly observed in *operando* optical microscopy<sup>3</sup>. In a hybrid mechanism, electronic conductivity could facilitate internal plating at pores near the Li-LLZO interface which then couples to fracture once the pore is completely filled<sup>27</sup>. The difficulty of rigorously testing these hypotheses arises from the ill-defined nature of the lithium metal–LLZO interface. For example, unknown electrode geometries due to void formation on the stripping electrode in macroscopic lithium electrodes results in uncertain contact potentials for symmetric cells<sup>28,29</sup>. Chemically, carbonate contamination due to reactions with ambient moisture and CO<sub>2</sub><sup>30,31</sup> and the use of lithium-metal foils with surface organics and oxides<sup>32,33</sup> further contribute to the complexity of the interface between lithium metal and LLZO. These complexities lead us to conclude that, similar to other material failure, lithium intrusion needs to be interrogated statistically.

In this work, we systematically tested the hypothesis that mechanical flaws in the solid electrolyte are the microstructural defects responsible for intrusion initiation. To ensure sufficient statistics, we conducted 48 lithium plating experiments on pristine LLZO without air exposure. Specifically, we employed *operando* SEM microelectrode methods<sup>11,34</sup> while controlling the contact force between the microprobe and LLZO surface. Combining these statistics with electrochemical modeling, we found that the intrusion probability as a function of lithium metal diameter follows a Weibull distribution, suggesting a defect-driven intrusion initiation mechanism. We observed that a high mechanical loading (5 mN vs. 0.1 mN) dramatically increases the likelihood of intrusion events, causing more intrusions at smaller electrode diameters. A combination of *ex situ* indentation measurements and finite element method (FEM) simulations suggests that nanoscale cracks likely initiate intrusion in LLZO. Furthermore, *operando* LLZO cantilever bending experiments revealed a strong mechanical strain effect on

regulating the propagation of intrusions. Our work establishes a method to quantify the effects of microstructural defects and mechanical strain on solid-state electrolytes and motivates the use of advanced characterization to further understand nanoscale defects in these complex systems.

## Results and discussion

### *Operando observation of lithium-intrusion initiation and electrochemical interpretation*

Figure 1 presents an overview of the experiment setup, a representative current-voltage curve, and *operando* SEM images of the lithium-plating process. In all experiments, we employ freshly fractured, phase-pure Ta-doped LLZO (transported from a dedicated LLZO glovebox to the SEM using an air-free transfer system) to ensure a chemically pristine interface, similar to previous work<sup>11</sup>. We acknowledge that this preparation route may lead to different defects on the surface compared to other preparation methods such as polishing or tape casting. To initiate each experiment, the tungsten microprobe is brought into contact with the LLZO surface in a region without any obvious microstructural defects (large pores, cracks, etc.). The contact force is quantified via a spring table located inside the SEM. Upon performing linear sweep voltammetry, we observe rapid growth of lithium-metal whiskers on the surface of the LLZO (at about  $V_{app} < |-0.1|$  V), as shown in Figure 1c.

As the applied potential is swept to more anodic potentials, the current increases non-linearly. At a critical  $V_{app}$ , metallic lithium is observed via SEM to induce cracks in the LLZO at some distance away from the probe, resulting in lithium intrusion. This typically occurs after the lithium whisker has reached many microns in diameter. These two lithium growth modes, pre-intrusion and post-intrusion, are shown in a tilted SEM image in Figure 1e, with the lithium metal whisker highlighted in red and intrusions highlighted in orange. Once the onset of

intrusions (indicating fracture) is visible in the SEM, we observe rapid propagation of intrusions on the LLZO surfaces with an accompanying increase in current magnitude (See Figure S1 for additional SEM images of intrusion morphology). We rule out electron-beam-induced effects (e.g., charging) since the electrochemistry as well as lithium and intrusion morphology proceed identically with the electron-beam turned off during plating. Importantly, large variation is observed in current and voltage at intrusion onset (see Figures S2 and S3).

To interpret the electrochemical data, we model two sources of overpotential: charge-transfer kinetics at the lithium–LLZO (working electrode) interface,  $\eta^{WE}$ , and the ohmic, semi-infinite constriction resistance<sup>11</sup> of the LLZO,  $\eta^{Ohm}$ . In this simple model, we assume that the lithium-LLZO contact is circular in shape and that the charge-transfer kinetics is symmetric Butler-Volmer in nature<sup>35,36</sup>. The applied potential,  $V_{app}$ , is given by:

$$V_{app} = \eta^{Ohm} + \eta^{WE} = \frac{i}{2\sigma_{ion}d} + \frac{2RT}{F} \operatorname{arcsinh}\left(\frac{j}{2j_0}\right) \quad (1)$$

where  $i$  is the current,  $d$  is the effective diameter of the lithium-LLZO contact,  $\sigma_{ion}$  is the ionic conductivity of LLZO,  $j$  is the areal current density, and  $j_0$  is the exchange current density (see the Supplemental Information for more details on the model). We employ this model to calculate the lithium whisker diameter ( $d$ ) from the electrochemical data, and Figure S4 shows a histogram of failure diameter values. From  $d$ , we then determine the current density and working electrode overpotential. The geometrically averaged current density at failure is extremely high with wide variation (Figure S5), significantly higher than reported for macroscopic lithium metal cells, which is consistent with previously reported observations<sup>11</sup>. Figure 2 presents the analysis for three typical experiments. As we discuss later,  $d$  and the current density are not sensitive to either the choice of the charge-transfer mechanism (i.e., Butler-Volmer) or the exchange current density, as  $\eta^{WE}$  is much smaller than  $\eta^{Ohm}$  in our experiments. Specifically, neglecting the charge-

transfer overpotential (second term) in Equation 1 translates only to a difference in the estimated whisker diameter of < 10%.

The lithium metal whisker diameter increases monotonically with  $V_{app}$  for all plating experiments. As shown in Figure 2b, the whisker diameter (at the interface with LLZO) grows from ~1 micron to over 10 microns before intrusions are observed. The diameter estimated by this model is somewhat smaller than lithium whisker diameter observed in SEM. However, the electrochemical estimate of the whisker diameter more accurately reflects the lithium-LLZO contact area than the area obtained by SEM imaging because there are a significant number of voids at the lithium-LLZO interface, as observed in focused-ion beam (FIB) cross-sectional SEM images in Figure S6.

The estimated value of the working electrode overpotential, in contrast to whisker diameter, does not change monotonically with applied potential (Figure 2d). Counterintuitively, for many experiments the estimated magnitude of  $\eta^{WE}$  actually decreases with applied potential. This occurs because the current density decreases as the whisker diameter grows. Therefore, the applied voltage primarily controls the diameter of the lithium whisker, rather than the charge-transfer overpotential. The magnitude of  $\eta^{WE}$  estimated by this method (typically tens of mV) is significantly smaller than the magnitude of  $V_{app}$  at fracture (typically 1 V), in agreement with previous literature on LLZO interfacial kinetics<sup>11</sup>, verifying that our results here are insensitive to the charge-transfer mechanism assumed in the model.

### ***Statistical analysis of intrusion initiation***

Using our force-controlled microprobe setup, we performed a total of 34 plating experiments to gather statistics on intrusion probability. Here,  $n = 11$  baseline experiments were

performed on pristine fractured LLZO at < 0.1 mN contact force. To quantify the likelihood of intrusion initiation, we fit an exponential power law (which has the same form as a two-parameter Weibull function) to the failure probability, commonly used in fracture mechanics<sup>37,38</sup>.

Mathematically, the cumulative failure probability is given by:

$$P_f = 1 - \exp\left[-\left(\frac{d_{fail}}{d_0}\right)^k\right] \quad (2)$$

where  $d_{fail}$  is the effective diameter of the lithium whisker at failure,  $d_0$  is the characteristic lithium diameter at which failure occurs for a given set of conditions, and  $k$  is a fitting parameter. The standard deviation of the fitted parameters was calculated using the bootstrapping scheme (see Methods)<sup>39</sup>. In this model, the parameters  $k$  and  $d_0$  provide quantitative metrics to compare the failure probabilities between different sample conditions, where a larger  $d_0$  implies a lower failure probability for a constant lithium whisker diameter, and a larger  $k$  value implies a tighter distribution of failure diameters. In addition, we emphasize that the exponent,  $k$  in this model is not the Weibull modulus typically reported in fracture mechanics literature. This is because the Weibull modulus quantifies the variability in failure strength under constant sample geometry. Here, we are instead quantifying the variability in sample geometry (lithium whisker diameter) at failure rather than the strength.

Figure 3a shows the cumulative failure probability as a function of the estimated lithium whisker diameter, along with the fitted model parameters. We observe a strong correlation between whisker size and failure probability, as evidenced by the linear relationship and fit in Figure 3a. The strong correlation of lithium whisker size to the failure probability is similar to failure size effects in other fields such as fracture of brittle materials<sup>37</sup> and dielectric breakdown in semiconductor gate oxides<sup>40</sup>. In these fields, the size dependence emerges as a result of defects

in the materials which are randomly distributed throughout the sample. The similar statistical relationships observed here suggest that the initiation of lithium intrusions is defect-driven with the mechanism illustrated in Figure 3b. In this proposed mechanism, the diameter of a lithium whisker grows continuously until the whisker interacts with a defect, which consequently initiates intrusion growth. For samples with similar  $k$  values,  $d_0$  provides a quantitative description of the defect density in the material, with higher  $d_0$  indicating a lower defect density, and vice versa. The analysis here could also be re-framed in terms of lithium whisker area at failure instead of diameter, with no loss of generality. With this defect-driven interpretation of the failure statistics, next we quantify how mechanical loading affects the probability of intrusion initiation.

### ***High microprobe contact force increases intrusion likelihood***

To test the hypothesis that localized microstructural defects initiate lithium intrusions, we engineered controlled defects into the surface of the LLZO. The most consistent method of initiating lithium intrusions was by damaging the LLZO surface via microprobe loading. Figure 3a shows the change in the cumulative distribution function between the 0.1 and 5 mN load conditions for  $n = 11$  and  $n = 23$  experiments performed, respectively. There is a clear distinction between the two loadings, with the higher loading force decreasing  $d_0$  (characteristic diameter at which intrusion occurs) from  $11 \pm 2 \mu\text{m}$  to  $4.2 \pm 0.6 \mu\text{m}$ . Furthermore,  $d_0$  for the 5 mN contact is similar in size to the estimated contact region of the tungsten probe (discussed later). In addition, SEM images in Figure S1 confirm the substantial decrease in whisker size at failure, with electrochemical data for all experiments shown in Figure S3. We observe that this effect is present regardless of whether the probe contact force is persistent through the entire plating

process (orange circular points) or if the probe first contacted the surface at high force, retracted, and then re-contacted to the surface at  $< 0.1$  mN in the same location (orange squares). This finding implies that the higher contact force causes irreversible damage to LLZO, leading to changes in the intrusion behavior. We note that our measurement of the contact force does not include the lateral component (sliding force) but only the surface normal component.

The data shown in Figure 3 for the 5 mN contact force displays some deviation from the linear trend at low values of failure diameter. This makes intuitive sense from a defect density perspective, as the defects generated by the high contact force cluster around the probe, yielding non-uniform defect densities resulting in deviations from the Weibull model. Such clustering is more clearly observed in the electrochemical data and the linear scale histogram of failure diameters shown in Figures S3 and S4.

In contrast to the microprobe-induced defects, our attempt to generate defects via FIB milling and scratching the surface with a diamond scribe were unsuccessful. Even a small exposure of the LLZO surface to the  $\text{Ga}^+$ -ion beam was sufficient to completely prevent lithium metal from being deposited on the surface of LLZO, possibly due to amorphization of the surface. Macroscopic scratches resulted in significantly different lithium-plating kinetics, making comparisons between the pristine LLZO surface and the damaged surface unapplicable.

To summarize, a large contact force between the tungsten probe and LLZO surface increases the intrusion likelihood due to irreversible damage induced by the probe. However, SEM imaging did not reveal notable morphological damage on the surface, a point which we explore in the next section.

### ***Micron-scale sample morphology does not correlate to intrusion morphology***

To gain a better understanding of correlations between microstructure features and intrusion initiation, we examined the sub-surface LLZO morphology using FIB cross-sectional milling before and after intrusions in the same microscope. For the pristine LLZO (without any electrochemistry performed), the subsurface FIB milling revealed a small number of pores ( $\sim 0.5 \mu\text{m}$  in diameter) as well as some regions of SEM contrast (see Figure S7 for images). Some of these pores are partially filled with an unknown material, even before any lithium plating occurred, possibly from impurities in the material or generated from FIB damage. We also examined the surface and subsurface morphology after application of a 5 mN force using the tungsten microprobe, but prior to lithium plating. As shown in Figures S7 and S8, we did not observe large changes in morphology upon contact, either on or below the surface after FIB milling. However, upon repeated indentation at high forces, we did observe chipping of the surface.

Figure 4 shows high-resolution SEM images of lithium intrusions in plan-view and cross section geometries after electrochemistry was performed. After lithium intrusions appear in the LLZO, narrow cracks are observed within the solid electrolyte, as shown in Figure 4b. At most locations, the cracks are barely visible via SEM with crack widths  $< 30 \text{ nm}$ . From the FIB cross section, we did not observe a significant change in porosity, or any lithium metal isolated from the crack network.

Overall, our post-mortem FIB characterization did not reveal obvious morphological features that correlate with the initiation of intrusions. Specifically, we did not observe connections between the intrusion crack network and sub-surface pores. Some cracks appeared

to follow grain-boundary paths; however, others appeared to propagate through the grain interior (see Figure S9), similar to other literature results on both single and polycrystalline LLZO<sup>41,42</sup>.

Given the high speed of crack growth and narrow crack widths in LLZO, it is challenging to obtain more insight by directly observing the intrusion initiation process in SEM. Because of this, we examined the different mechanical damage modes to correlate various types of mechanical defects to our electrochemical observations.

### ***Contact damage modes from tungsten microprobe***

To study the mechanical effect of the microprobe contact, we performed *ex situ* nanoindentation on polished LLZO using a spherical diamond tip with a diameter of 3.6 μm. The hysteresis in load–displacement curves shown in Figure 5 indicates that plastic deformation may be occurring upon 5 mN contact. In addition, microfracture could also simultaneously occur upon loading, as commonly observed in many ceramics during wear and abrasion testing<sup>43–45</sup>.

To examine the possibility of plastic deformation upon loading, we conducted FEM simulations using elastic and elastic-plastic constitutive relations to model both the *ex situ* diamond spherical indentation as well as the tungsten microprobe used in the operando SEM experiments. Considering a LLZO hardness of about 8 GPa<sup>46</sup>, we expect plastic deformation to occur at a yield strength of between 5-8 GPa<sup>47</sup>. Both elastic and elastic-plastic FEM simulations of diamond indentation result in a poor fit to the experimental results. This suggests that plastic deformation alone cannot explain the observed deviations from elastic behavior in the load curve. It is likely that micro/nano-scale fracture events are instead responsible for the decrease in slope. Other damage modes such as phase transformation may also influence the loading curve,

but experimental data is lacking to understand how large this effect may be. See Figure S10 for more load-displacement curves.

FEM simulations of indentation using the tungsten microprobe resulted in yielding of the tungsten tip at an applied load of 5 mN. This limited the maximum stress in the LLZO to < 3 GPa, as shown in Figure 5b. These simulations suggest that minimal-to-no plastic deformation is occurring in the LLZO upon tungsten contact, and that plastic deformation in LLZO is not responsible for the shift in intrusion behavior shown in Figure 3. The experimental observation of significant deformation of the tungsten microprobe upon contact with the LLZO surface (as shown in Figure S11) suggests that the microprobe yields before the LLZO does.

We also employed FEM simulations to quantitatively compare the electrochemically measured diameter of the lithium whisker at failure to the length scale of mechanical damage in LLZO. Figure 5b shows that the characteristic failure diameter for the 5 mN contact force experiments is similar in size to the region of the LLZO sample with stress above 100 MPa. Given that previous literature estimates a macroscopic fracture stress of LLZO also in the ~100 MPa<sup>46</sup> range, the agreement in length scale between the electrochemical measurement and mechanical simulation also suggests that fracture events are causing the change in intrusion behavior shown in Figure 3.

Overall, our results indicate that plastic deformation is unlikely to be occurring upon tungsten microprobe loading, suggesting fracture as a more likely damage mechanism. Therefore, we conclude that cracks are the most likely defect responsible for the decrease in characteristic failure diameter shown in Figure 3. However, such cracks responsible for lithium-intrusion initiation are not detectable using standard microscopy techniques, such as SEM or optical imaging. Recent TEM imaging of crack formation in Al<sub>2</sub>O<sub>3</sub> highlights that cracks may be

only a few nanometers in width<sup>48</sup>, posing a challenge for non-destructive characterization of LLZO surfaces.

### ***Mechanical strain regulates intrusion propagation***

To further reveal the mechanical origin of lithium metal intrusions, we conducted *operando* SEM microprobe experiments on a strained LLZO cantilever. As schematically shown in Figure 6a, a 15 mm-long LLZO cantilever (attached to a thin layer of lithium and copper) was clamped at one end and pushed upward at the free end. This setup results in a linear variation in strain along the length of the cantilever, in which there is zero strain at the free end and maximum strain at the clamped end. This geometry enables different mechanical strains to be probed along the same cantilever.

As in the earlier experiments, we observe lithium intrusion at various compressive stresses while flowing ionic current between the top and the bottom surface of the cantilever. Figure 6b reveals that lithium intrusions do not have a preferred direction at 0% strain (free end of cantilever), indicating the random nature of the pre-existing defect distribution. At 0.033% compressive strain (the middle of the cantilever), the lithium intrusions start to show more geometric alignment as shown in Figure 6c. Strikingly, at the base of the cantilever where the compressive strain is only ~0.070%, the intrusions exhibit a strong directionality along the cantilever longitudinal direction, i.e., along the compressively strained direction (see Figure 6d and Figure S12). Tests were consistently performed in the low contact force regime ( $0.1 \pm 0.03$  mN). To rule out the possibility that the rotational angle between the microprobe and sample influences the intrusion direction, we conducted experiments on a cantilever that was rotated 20 and 45 degrees relative to the probe (Figures 6e,f) and found lithium intrusions remained predominantly aligned along the cantilever longitudinal direction rather than perpendicular to the

microprobe. We propose that the directional propagation of intrusions occurs because the uniaxial compression facilitates crack closure and increases the effective fracture toughness in the transverse direction. Recently, the stress influence on the in-plane propagation of lithium within the solid electrolyte was also observed via optical microscopy<sup>49</sup>. These results show that mechanical strain controls the propagation of intrusions after their initiation and provides further evidence of the mechanical origin of lithium metal intrusions.

### ***Electronic conductivity considerations***

Previous work using neutron depth profiling and SEM data has argued that electronic conductivity in LLZO causes isolated lithium plating within the bulk, even as deep as 500  $\mu\text{m}$ <sup>24</sup>. In our 48 SEM microprobe experiments, however, we did not observe any lithium nucleation at the surface isolated from the whisker growth (within the resolution of SEM). This implies that the electronic conductivity of LLZO was low. In certain cases, multiple whiskers grow when the initial whisker re-contacts the surface at an alternate location, which is not due to electronic leakage in the solid electrolyte. Post-mortem FIB cross sectioning (shown in Figure 4) did not reveal any lithium metal that was not connected to the crack network. This suggests that even if lithium metal is deposited below the surface, the resulting intrusions are still closely connected to mechanical fracture processes. Our results are consistent with recent *operando* optical imaging<sup>3</sup> which observed lithium intrusion growth originating near the electrode surface, rather than within the bulk.

We also ruled out changes in electronic conductivity upon mechanical deformation by considering the effect of each damage mode. Of the two damage modes discussed here, fracture and plastic deformation, the latter is more likely to alter the transport properties, because of the

introduction of atomic-scale defects such as dislocations<sup>50</sup>. However, based on our mechanics simulations we do not believe plastic deformation occurs in the LLZO upon contact with the tungsten microprobe. Moreover, in the cantilever bending experiments a strain of less than 0.070% at the surface is also not expected to induce significant variations in transport properties of LLZO<sup>51</sup>. Therefore, we conclude that it is unlikely that increases in electronic conductivity are leading to the observed changes in the intrusion behavior.

## Conclusions

In this work, the mechanism for lithium intrusions to initiate on LLZO surfaces was examined using *operando* SEM microprobe. The cumulative probability of intrusion initiation as a function of lithium whisker diameter was shown to follow a Weibull distribution. This finding suggests that the intrusion initiation process is facilitated by localized defects within the LLZO. In addition, we discovered that the probability distribution is dramatically shifted by varying the contact force between the tungsten microprobe and LLZO surface. *Ex situ* diamond-tip indentation showed significant deviation from an elastic-plastic response, suggesting that microcracking is occurring in the sample. Further, FEM analysis of the microprobe-LLZO contact suggested that plastic deformation in LLZO is unlikely. *Operando* LLZO cantilever bending experiments revealed that intrusion propagation is strongly influenced by compressive strain of only ~0.070%. Based on these results, we conclude that nanocracks (either pre-existing ones or those generated via external loads) are the origin of lithium-metal intrusions in LLZO and their propagation behavior can be controlled by mechanical strain. We emphasize that these microcracks are difficult to observe using standard microscopy techniques such as SEM or optical imaging and look to the development of advanced characterization methods to study

these defects. Overall, the mechanisms examined here provide a foundation for understanding the complex interactions between the chemical, electrical, and mechanical forces that govern lithium-intrusion processes in solid-state electrolytes.

## References

1. Chen, Y. *et al.* Understanding the lithium dendrites growth in garnet-based solid-state lithium metal batteries. *J. Power Sources* **521**, 230921 (2022).
2. Frenck, L., Sethi, G. K., Maslyn, J. A. & Balsara, N. P. Factors That Control the Formation of Dendrites and Other Morphologies on Lithium Metal Anodes. *Front. Energy Res.* **7**, 115 (2019).
3. Kazyak, E. *et al.* Li Penetration in Ceramic Solid Electrolytes: Operando Microscopy Analysis of Morphology, Propagation, and Reversibility. *Matter* **2**, 1025–1048 (2020).
4. Monroe, C. & Newman, J. The Impact of Elastic Deformation on Deposition Kinetics at Lithium/Polymer Interfaces. *J. Electrochem. Soc.* **152**, A396 (2005).
5. Ni, J. E., Case, E. D., Sakamoto, J. S., Rangasamy, E. & Wolfenstine, J. B. Room temperature elastic moduli and Vickers hardness of hot-pressed LLZO cubic garnet. *J. Mater. Sci.* **47**, 7978–7985 (2012).
6. Yu, S. *et al.* Elastic Properties of the Solid Electrolyte Li<sub>7</sub>La<sub>3</sub>Zr<sub>2</sub>O<sub>12</sub> (LLZO). *Chem. Mater.* **28**, 197–206 (2016).
7. Lu, Y. *et al.* Critical Current Density in Solid - State Lithium Metal Batteries: Mechanism, Influences, and Strategies. *Adv. Funct. Mater.* **31**, 2009925 (2021).
8. Fu, C. *et al.* Universal chemomechanical design rules for solid-ion conductors to prevent dendrite formation in lithium metal batteries. *Nat. Mater.* **19**, 758–766 (2020).

9. Zheng, H. *et al.* Intrinsic Lithiophilicity of Li–Garnet Electrolytes Enabling High-Rate Lithium Cycling. *Adv. Funct. Mater.* **30**, 1906189 (2020).
10. Hitz, G. T. *et al.* High-rate lithium cycling in a scalable trilayer Li-garnet-electrolyte architecture. *Mater. Today* **22**, 50–57 (2019).
11. Krauskopf, T. *et al.* The Fast Charge Transfer Kinetics of the Lithium Metal Anode on the Garnet - Type Solid Electrolyte  $\text{Li}_{6.25}\text{Al}_{0.25}\text{La}_3\text{Zr}_2\text{O}_{12}$ . *Adv. Energy Mater.* **10**, 2000945 (2020).
12. Ma, C. *et al.* Interfacial Stability of Li Metal–Solid Electrolyte Elucidated via in Situ Electron Microscopy. *Nano Lett.* **16**, 7030–7036 (2016).
13. Connell, J. G. *et al.* Kinetic versus Thermodynamic Stability of LLZO in Contact with Lithium Metal. *Chem. Mater.* **32**, 10207–10215 (2020).
14. Tippens, J. *et al.* Visualizing Chemomechanical Degradation of a Solid-State Battery Electrolyte. *ACS Energy Lett.* **4**, 1475–1483 (2019).
15. Wenzel, S. *et al.* Direct Observation of the Interfacial Instability of the Fast Ionic Conductor  $\text{Li}_{10}\text{GeP}_2\text{S}_{12}$  at the Lithium Metal Anode. *Chem. Mater.* **28**, 2400–2407 (2016).
16. Porz, L. *et al.* Mechanism of Lithium Metal Penetration through Inorganic Solid Electrolytes. *Adv. Energy Mater.* **7**, 1701003 (2017).
17. Park, R. J.-Y. *et al.* Semi-solid alkali metal electrodes enabling high critical current densities in solid electrolyte batteries. *Nat. Energy* **6**, 314–322 (2021).
18. Schmidt, R. D. & Sakamoto, J. In-situ, non-destructive acoustic characterization of solid state electrolyte cells. *J. Power Sources* **324**, 126–133 (2016).

19. Barroso-Luque, L., Tu, Q. & Ceder, G. An Analysis of Solid-State Electrodeposition-Induced Metal Plastic Flow and Predictions of Stress States in Solid Ionic Conductor Defects. *J. Electrochem. Soc.* **167**, 020534 (2020).
20. Klinsmann, M., Hildebrand, F. E., Ganser, M. & McMeeking, R. M. Dendritic cracking in solid electrolytes driven by lithium insertion. *J. Power Sources* **442**, 227226 (2019).
21. Bucci, G. & Christensen, J. Modeling of lithium electrodeposition at the lithium/ceramic electrolyte interface: The role of interfacial resistance and surface defects. *J. Power Sources* **441**, 227186 (2019).
22. De Jonghe, L. C., Feldman, L. & Beuchele, A. Slow degradation and electron conduction in sodium/beta-aluminas. *J. Mater. Sci.* **16**, 780–786 (1981).
23. Feldman, L. A. & De Jonghe, L. C. Initiation of mode I degradation in sodium-beta alumina electrolytes. *J. Mater. Sci.* **17**, 517–524 (1982).
24. Han, F. *et al.* High electronic conductivity as the origin of lithium dendrite formation within solid electrolytes. *Nat. Energy* **4**, 187–196 (2019).
25. Liu, X. *et al.* Local electronic structure variation resulting in Li ‘filament’ formation within solid electrolytes. *Nat. Mater.* **20**, 1485–1490 (2021).
26. Dong, Y., Zhang, Z., Alvarez, A. & Chen, I.-W. Potential jumps at transport bottlenecks cause instability of nominally ionic solid electrolytes in electrochemical cells. *Acta Mater.* **199**, 264–277 (2020).
27. Tu, Q., Shi, T., Chakravarthy, S. & Ceder, G. Understanding metal propagation in solid electrolytes due to mixed ionic-electronic conduction. *Matter* **4**, 3248–3268 (2021).
28. Kasemchainan, J. *et al.* Critical stripping current leads to dendrite formation on plating in lithium anode solid electrolyte cells. *Nat. Mater.* **18**, 1105–1111 (2019).

29. Raj, V. *et al.* Direct correlation between void formation and lithium dendrite growth in solid-state electrolytes with interlayers. *Nat. Mater.* (2022) doi:10.1038/s41563-022-01264-8.
30. Sharafi, A. *et al.* Surface Chemistry Mechanism of Ultra-Low Interfacial Resistance in the Solid-State Electrolyte Li<sub>7</sub>La<sub>3</sub>Zr<sub>2</sub>O<sub>12</sub>. *Chem. Mater.* **29**, 7961–7968 (2017).
31. Orera, A., Larraz, G., Rodríguez-Velamazán, J. A., Campo, J. & Sanjuán, M. L. Influence of Li<sup>+</sup> and H<sup>+</sup> Distribution on the Crystal Structure of Li<sub>7-x</sub>H<sub>x</sub>La<sub>3</sub>Zr<sub>2</sub>O<sub>12</sub> (0 ≤ x ≤ 5) Garnets. *Inorg. Chem.* **55**, 1324–1332 (2016).
32. Otto, S.-K. *et al.* In-Depth Characterization of Lithium-Metal Surfaces with XPS and ToF-SIMS: Toward Better Understanding of the Passivation Layer. *Chem. Mater.* **33**, 859–867 (2021).
33. Meyerson, M. L. *et al.* The effect of local lithium surface chemistry and topography on solid electrolyte interphase composition and dendrite nucleation. *J. Mater. Chem. A* **7**, 14882–14894 (2019).
34. Zhao, J. *et al.* In situ Observation of Li Deposition - Induced Cracking in Garnet Solid Electrolytes. *ENERGY Environ. Mater.* eem2.12261 (2021) doi:10.1002/eem2.12261.
35. Tian, H.-K., Liu, Z., Ji, Y., Chen, L.-Q. & Qi, Y. Interfacial Electronic Properties Dictate Li Dendrite Growth in Solid Electrolytes. *Chem. Mater.* **31**, 7351–7359 (2019).
36. Ji, X. *et al.* Solid-State Electrolyte Design for Lithium Dendrite Suppression. *Adv. Mater.* **32**, 2002741 (2020).
37. Zok, F. W. On weakest link theory and Weibull statistics. *J. Am. Ceram. Soc.* **100**, 1265–1268 (2017).
38. Quinn, J. B. & Quinn, G. D. A practical and systematic review of Weibull statistics for reporting strengths of dental materials. *Dent. Mater.* **26**, 135–147 (2010).

39. Efron, B. & Tibshirani, R. *An introduction to the bootstrap*. (Chapman & Hall, 1993).
40. Wu, E. Y. & Vollertsen, R.-P. On the weibull shape factor of intrinsic breakdown of dielectric films and its accurate experimental determination-part I: theory, methodology, experimental techniques. *IEEE Trans. Electron Devices* **49**, 2131–2140 (2002).
41. Cheng, E. J., Sharafi, A. & Sakamoto, J. Intergranular Li metal propagation through polycrystalline Li<sub>6.25</sub>Al<sub>0.25</sub>La<sub>3</sub>Zr<sub>2</sub>O<sub>12</sub> ceramic electrolyte. *Electrochimica Acta* **223**, 85–91 (2017).
42. Swamy, T. *et al.* Lithium Metal Penetration Induced by Electrodeposition through Solid Electrolytes: Example in Single-Crystal Li<sub>6</sub>La<sub>3</sub>ZrTaO<sub>12</sub> Garnet. *J. Electrochem. Soc.* **165**, A3648–A3655 (2018).
43. Mukhopadhyay, A. K., Chakraborty, D., Swain, M. V. & Mai, Y.-W. Scratch deformation behaviour of alumina under a sharp indenter. *J. Eur. Ceram. Soc.* **17**, 91–100 (1997).
44. Swain, M. V. Microfracture about scratches in brittle solids. *Proc. R. Soc. Lond. Math. Phys. Sci.* **366**, 575–597 (1979).
45. Xu, H. H. K. & Jahanmir, S. Microfracture and material removal in scratching of alumina. *J. Mater. Sci.* **30**, 2235–2247 (1995).
46. Yan, G. *et al.* An investigation on strength distribution, subcritical crack growth and lifetime of the lithium-ion conductor Li<sub>7</sub>La<sub>3</sub>Zr<sub>2</sub>O<sub>12</sub>. *J. Mater. Sci.* **54**, 5671–5681 (2019).
47. Swab, J. J. *et al.* Knoop Hardness-Apparent Yield Stress Relationship in Ceramics. *Int. J. Appl. Ceram. Technol.* **9**, 650–655 (2012).
48. Kondo, S., Ishihara, A., Tochigi, E., Shibata, N. & Ikuhara, Y. Direct observation of atomic-scale fracture path within ceramic grain boundary core. *Nat. Commun.* **10**, 2112 (2019).

49. Chiang, Y.-M. Failure Mechanisms for Lithium Metal Anodes. Batteries Gordon Research Conference, Ventura, CA (2022).
50. Adepalli, K. K., Yang, J., Maier, J., Tuller, H. L. & Yildiz, B. Tunable Oxygen Diffusion and Electronic Conduction in SrTiO<sub>3</sub> by Dislocation - Induced Space Charge Fields. *Adv. Funct. Mater.* **27**, 1700243 (2017).
51. Qi, Y., Ban, C. & Harris, S. J. A New General Paradigm for Understanding and Preventing Li Metal Penetration through Solid Electrolytes. *Joule* (2020)  
doi:10.1016/j.joule.2020.10.009.
52. Reiser, J. *et al.* Ductilisation of tungsten (W): On the increase of strength AND room-temperature tensile ductility through cold-rolling. *Int. J. Refract. Met. Hard Mater.* **64**, 261–278 (2017).

### ***Acknowledgements***

This work was supported by the Samsung Advanced Institute of Technology. Some characterization aspects of the work were supported by the Assistant Secretary for Energy Efficiency, Vehicle Technologies Office of the US Department of Energy under the Advanced Battery Materials Research Program. T.C. and X.W.G. acknowledge financial support from StorageX Initiative at Stanford University. We thank Richard Chin, Juliet Jamtgaard, and Lorenz Lechner for assistance with installing and operating the microprobe system. We also thank Melody Wang, Ottman Tertuliano, Nick Rolston and William Nix, Lincoln Miara and Srinath Chakravarthy for helpful discussions. Finally, we thank Xiao Cui, Harry Thaman, and Swati Narasimhan for helpful discussions and comments on the manuscript. Part of this work was performed at the Stanford Nano Shared Facilities (SNSF), supported by the National Science

Foundation under award ECCS-2026822. This material is based on work supported by the National Science Foundation Graduate Research Fellowship under Grant No. 1656518.

### **Author contributions**

G.M., X.X. and T.C. performed most of the experiments and their analysis. E.B. and S.W. assisted with LLZO sample preparation and EIS measurement. E.K. assisted with electrical measurement and data analysis. C.M. Performed X-ray diffraction measurements and analysis. X.W.G. supervised and assisted with the design of cantilever bending experiments and FEM simulations. G.M., X.X. and W.C.C. designed the research plan. G.M., X.X., T.C., and W.C.C. wrote the manuscript with input from all authors.

## **Experimental Methods**

### ***Materials***

Ta-doped LLZO ( $\text{Li}_{6.6}\text{La}_3\text{Ta}_{0.4}\text{Zr}_{1.6}\text{O}_{12}$ ) was purchased from Toshima Corp. The materials were manufactured using a hot-press technique to ensure a high density (>99%) of the material. A powder X-ray diffraction pattern of the as-received pellets is presented in Figure S13. Elemental composition analysis provided by Toshima indicates that less than 0.01% by weight Fe, Ca, and Cr are present in the material. Lithium-metal foil (purity >99.9%) was purchased from Alfa Aesar.

### ***SEM microprobe electrochemical cell construction***

To ensure that the surface of the LLZO pellet was as clean as possible, we first fractured a 2-mm-thick LLZO pellet inside a dedicated Ar-filled glovebox, as performed in other work<sup>11</sup>.

The pellet was then hand-pressed onto a lithium-foil counter electrode (applied pressure >1 MPa) with the fractured surface visible. The lithium foil was supported by a stainless-steel sample holder that also served as the current collector. The sample was then loaded into a custom-built mechanical air-free sample transfer system to transport between the glovebox and a FEI Helios NanoLab 600i FIB/SEM system. The air-free transfer system was observed to have water and oxygen contaminants lower than 0.5 ppm, verified by observing a lack of color change in lithiated graphite ( $\text{LiC}_6$ ) which was held in the vessel for 45 min. The microprobe system consisted of a Kleindiek MM3A manipulator and a Ted Pella tungsten microprobe (for Autoprobe 100 & 200, taper angle of  $10^\circ$ ). A Bio-logic portable potentiostat (SP 300 or SP 240) was connected to the stainless-steel current collector and microprobe via an electrical feedthrough in the FIB/SEM system. The tungsten probe acted as the working electrode, and the lithium-metal foil served as the counter electrode in a two-electrode cell configuration. The tungsten probe was cut using the FIB system to have the shape of a truncated cone with the terminal end having a diameter of 5–8  $\mu\text{m}$ . The sample holder was electrically isolated from the FIB/SEM stage and grounded to avoid any ground loop or static charging issues. The electronic resistance of the tungsten probe and sample stage combined was measured to be less than  $20 \Omega$ .

### ***Calibration of SEM microprobe contact force***

To estimate the force applied by the probe, a calibration was performed using a displacement technique. A “spring table”, which is an SEM stage containing a well-calibrated spring (Kleindiek), was used to convert vertical motion of the sample into an applied force. A sample of LLZO was mounted to this stage, and the microprobe was contacted to the sample surface until a lateral probe displacement was observed similar to the electrochemical

experiments (5–10  $\mu\text{m}$ ). During the loading process, the sample was viewed at a  $45^\circ$  angle to observe the vertical displacement of the sample as well. The vertical displacement was converted to a force using the spring constant of the spring table.

### ***Electrochemical test procedure***

To deposit lithium metal, we performed linear sweep voltammetry experiments starting at 0 V vs. Li metal and at a constant sweep rate of 5 mV/s in the anodic direction. Lithium was observed to deposit at low-magnitude applied potentials of  $V_{onset} = -0.07 \pm 0.12$  V. The magnitude of the cell potential was increased until lithium-metal intrusions were observed to grow, which we define as failure. Once the experiment was completed, the microprobe was cleaned of residual lithium metal by mechanically brushing the probe onto a rubber O-ring, which was part of the sample-transfer system. For especially difficult-to-remove lithium metal, the Ga FIB was used to assist in cleaning the probe or cutting it to remove the lithium. The electrochemical experiment was then repeated for various conditions discussed below. The Ga FIB was also used to cut the probe to the desired shape for high-force contact experiments.

### ***Statistical analysis of failure diameter data***

The cumulative failure probability,  $P_f$ , was calculated by first sorting the data by the effective diameter at failure,  $d$ , from smallest to largest. Then, each data point was assigned an index,  $i = 1, 2, 3, \dots$ . The cumulative probability was calculated using the following equation:  $P_f = (i-0.5)/n$ , where  $n$  is the number of samples<sup>38</sup>. The standard deviation of the fitted parameters was calculated using the bootstrapping scheme<sup>39</sup>. Briefly, the original dataset was sampled with replacement, generating a new synthetic dataset with the same number of datapoints as the

original. Then, the fitting procedure was performed, and the parameters were computed. This process was repeated 1,000 times to generate a range of fitting parameters, from which the standard deviation was computed. Fitting was performed using least-squares linear regression using the statsmodels package in conjunction with Pandas and numpy packages in Python 3.8.

### ***Ex situ indentation methods***

Mechanical indentation measurements were performed on an iMicro indentation system (Nanomechanics) using a 3.6- $\mu\text{m}$  diameter spherical diamond tip. Tests were performed under active N<sub>2</sub> flow to mitigate air exposure. Loading and unloading were performed using a load-controlled indentation strain rate ( $\dot{P}/P$ ) of 1 s<sup>-1</sup>.

Because of the inconsistent results of indentation on a rough, fractured surface of LLZO, we elected to polish the samples to obtain more consistent results. The LLZO samples were polished for indentation using 400 and 800 grit silicon carbide sandpaper (Allied) for 2 and 5 min, respectively, followed by 6  $\mu\text{m}$  and 1  $\mu\text{m}$  diamond suspensions (Ted Pella) for 10 and 5 min, respectively. All the suspensions used glycol as the solvent. Polishing was performed by hand on an 8-inch-diameter polishing wheel (Buehler) at 150 rpm. The sample was washed in ethanol after each suspension step.

### ***Finite element simulations***

The contact stress within LLZO was estimated using finite element analysis in ABAQUS package. For tungsten contact, the full elasto-plastic constitutive law of W was adopted from the literature<sup>52</sup> and considered in the model (Young's modulus  $E = 400$  GPa, the initial yield stress = 1.42 GPa, ultimate tensile strength = 1.73 GPa). For LLZO, we assumed a linear elastic-perfect

plastic constitutive law with  $E = 150$  GPa,  $\nu = 0.24^{6,46}$  and an assumed yield strength of 4.5 GPa. For diamond contact, the diamond tip has an elastic modulus of 1141 GPa, and Poisson's ratio of 0.07. The tip-LLZO contact was simplified as an axisymmetric model, and both the tip and LLZO were modelled using 8-node quadrilateral elements (CAX8R) with a fine mesh of 5 nm at the contact to ensure convergence. The color contour reveals the Von Mises stress.

### ***LLZO cantilever bending***

The LLZO used for the cantilever bending experiment was mechanically polished and heat treated before cutting into cantilevers. The polishing and heat treatment processes are the same as those used for sample preparation for the EIS measurements of ionic conductivity (see Supplemental Information). A LLZO cantilever of 15 mm × 3 mm × 1 mm was cut using a custom scoring and fracturing jig, and then hand-pressed onto a thin (~100 μm) lithium-on-copper foil. Due to the significantly higher elastic modulus and thickness of LLZO than lithium and copper, the contribution of the lithium and copper was neglected in strain calculation. The sample was installed on a 3D printed electronically conductive fixture made of polylactic acid. The bending force was applied by compressing a spring with stiffness of 3.15 N/mm. A long bolt was installed as a spring guide to avoid buckling. The outer diameter of the spring was selected to match the width of the cantilever to increase structural stability. The amount of compression was adjusted by tightening a nut on the bolt where the grounding wire is also connected. It is noted that there was about one min of air exposure when installing the bending setup into the SEM. The compressive strain  $\varepsilon(x)$  at the top surface of the cantilever is calculated using Euler

beam theory, in which  $\varepsilon(x) = \frac{6Fx}{Eb^2}$ , where  $F$  is the applied force,  $x$  is the distance from the free end,  $E$  is the elastic modulus of LLZO, and  $b$  and  $h$  are the width and thickness of the cantilever.

## Figures

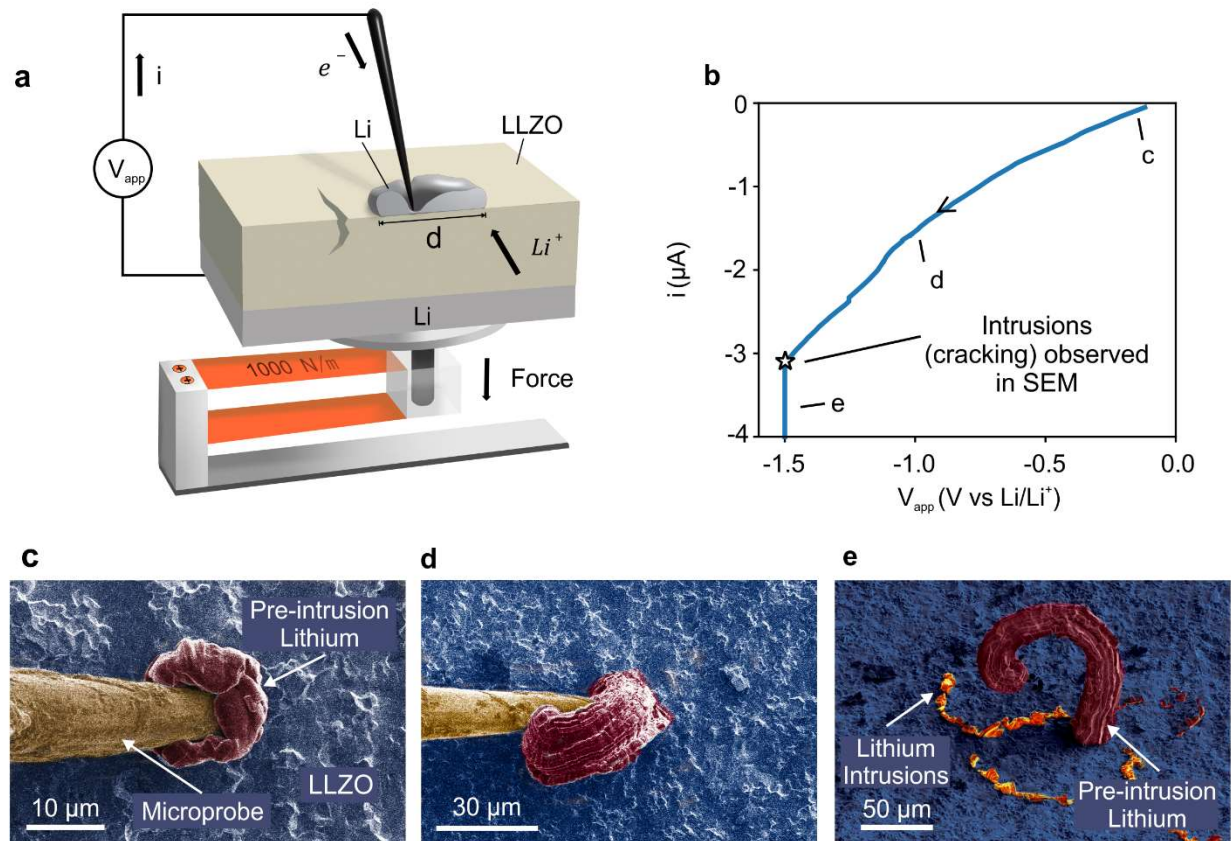


**Figure 1: Electroplating lithium metal onto LLZO via a force-controlled electrical microprobe inside SEM. (a)** Schematic of the force-controlled SEM microprobe experiment. **(b)** Representative result of a linear sweep voltammetry experiment. **(c-e)** Colorized *operando* SEM images of lithium plating experiments outlined in (a) with each image corresponding to the positions on plot (b).

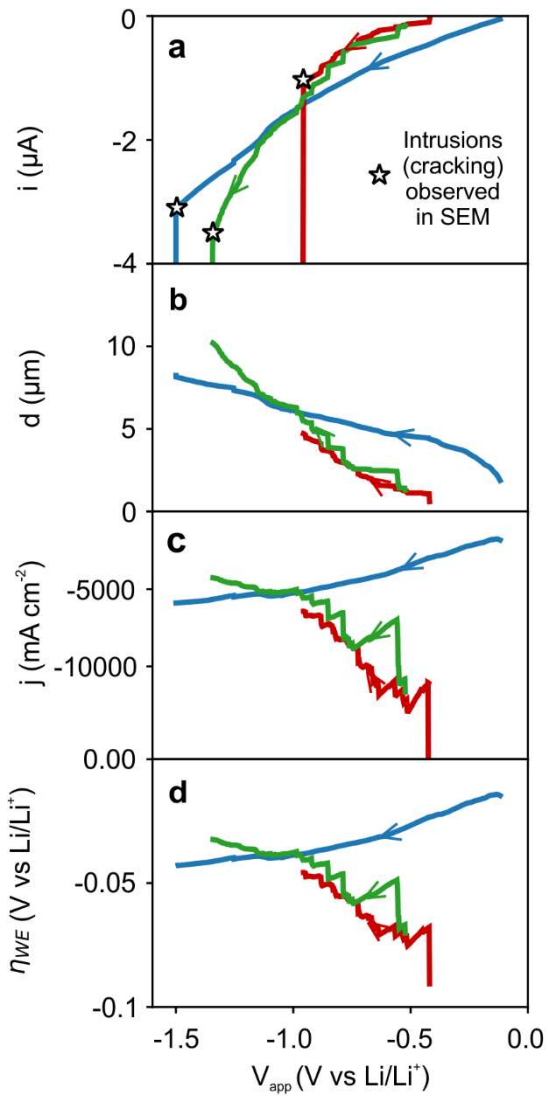


**Figure 2: Electrochemical analysis of three nominally identical SEM microprobe experiments as a function of applied potential (at a contact load of 0.1 mN).** (a) Measured current, (b) estimated effective diameter at Li–LLZO interface calculated using Equation 1, (c) estimated current density (area averaged) and (d) estimated charge-transfer overpotential. These parameters are computed for current between 50 nA and the spike when intrusion initiates.

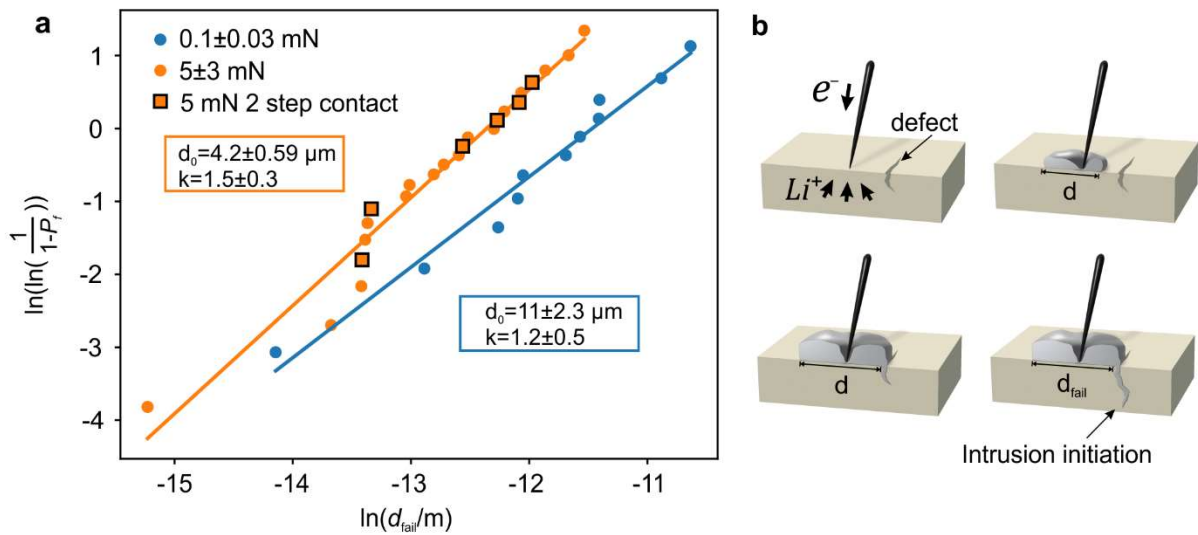


**Figure 3: Statistical analysis of intrusion initiation suggesting a defect-driven intrusion initiation mechanism.** (a) Statistical failure analysis of lithium-metal intrusion initiation in LLZO. Each data point corresponds to the lithium-metal diameter at intrusion initiation estimated from the electrochemical data. Blue: Low-contact-force SEM microprobe experiments ( $n = 11$  data points). Orange: High-contact-force SEM microprobe experiments ( $n = 23$ ). Orange squares: SEM microprobe experiments where a high contact force was first applied and subsequently re-contacted at a low force. (b) Schematic of proposed mechanism for lithium-metal intrusion into LLZO, highlighting the role of pre-existing surface defects.

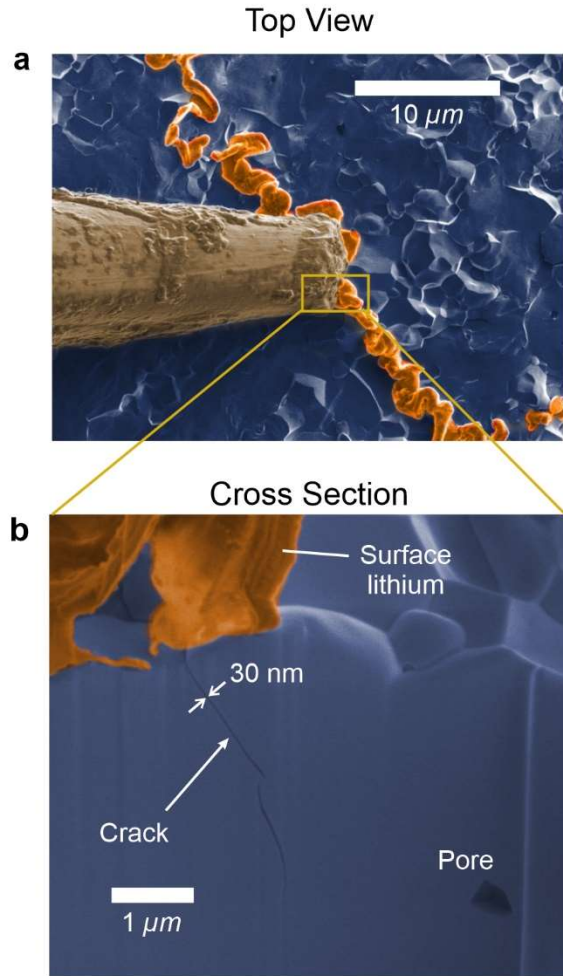


**Figure 4: SEM images of lithium intrusions after electrochemistry measurements.** (a) Top-view colorized SEM image of microprobe and lithium-metal intrusions. The orange box highlights the FIB cross-section region. (b) FIB cross section showing a narrow crack associated with intrusion processes. See Figure S6 for expanded set of FIB cross sections.

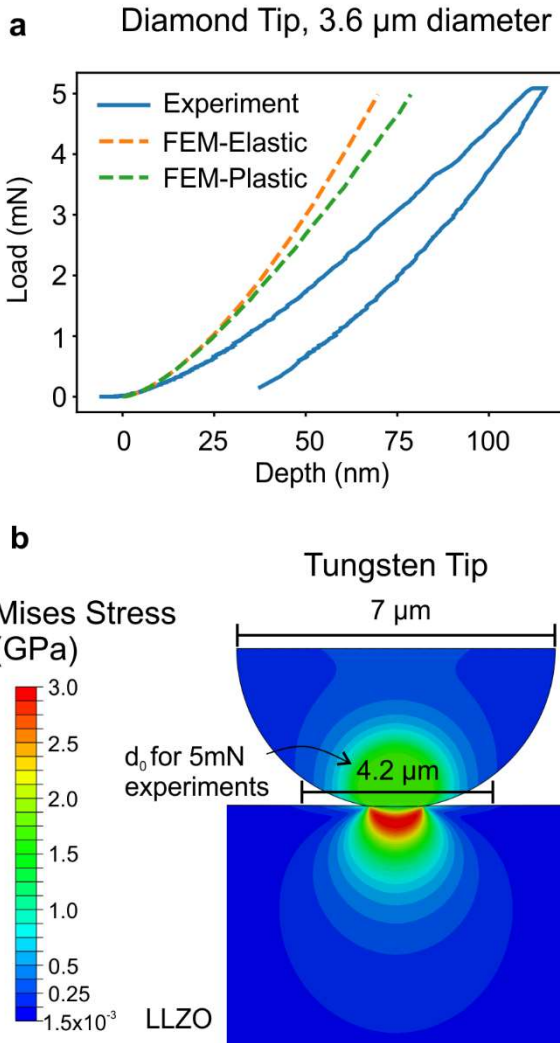


**Figure 5: Ex situ nanoindentation and FEM simulations analyzing the contact damage modes in LLZO from the tungsten microprobe. (a)** Spherical indentation load–displacement curves for polished LLZO samples using a 3.6  $\mu\text{m}$  diamond indenter. Dashed traces are FEM simulations using elastic or elastic-perfect plastic constitutive relations in the LLZO, with an assumed yield stress of 4.5 GPa. **(b)** FEM stress contours of 7  $\mu\text{m}$  diameter tungsten microprobe contact on LLZO incorporating yielding behavior of tungsten under 5 mN load. The characteristic failure diameter for lithium intrusions from Figure 3 is shown for comparison.

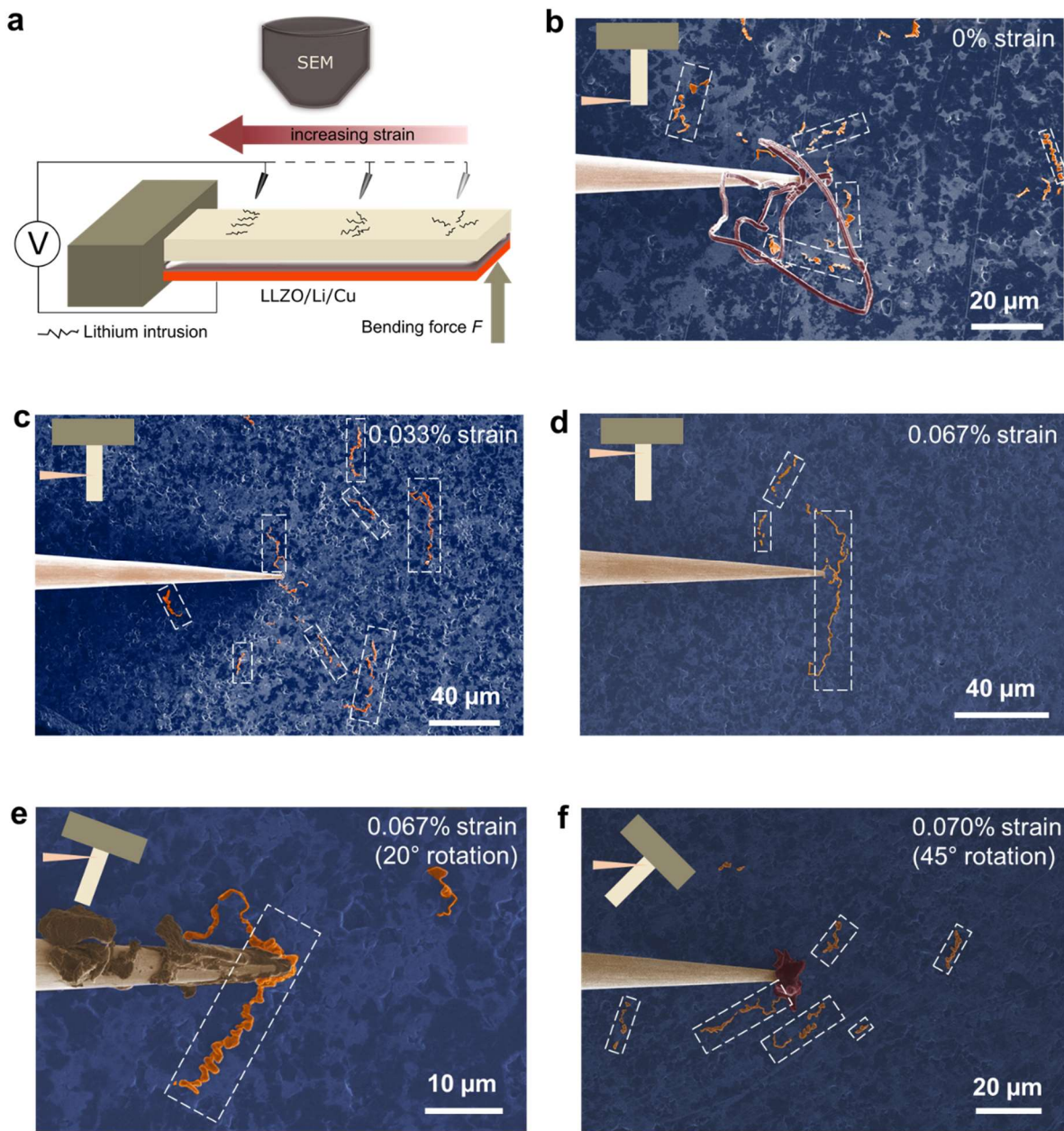


**Figure 6: *Operando* LLZO cantilever bending experiments revealing a strong mechanical strain effect on regulating the intrusion propagation behavior. (a)** Schematic of *operando* SEM microprobe experiment on bent LLZO cantilever. Colorized SEM images showing intrusions at **(b)** 0% strain (free end of the cantilever), **(c)** 0.033% strain (center of the cantilever), **(d, e)** 0.067% and **(f)** 0.070% strain (base of the cantilever). The intrusion propagates

in random directions at 0% strain and becomes gradually more aligned along the longitudinal direction of the cantilever with increasing compressive strain. (e, f) Intrusion propagation at 0.067% and 0.070% strain with the cantilever rotated by 20° and 45° relative to the microprobe. The intrusion propagation direction remains along the cantilever.